

Controller-decoder system requirements, derived by implementing Shor’s algorithm with surface codes

Yaniv Kurman¹, Lior Ella¹, Nir Halay¹, Oded Wertheim¹, and Yonatan Cohen¹

¹*Quantum Machines Inc., Tel Aviv, Israel*

Quantum Error Correction (QEC) is widely regarded as the most promising path towards quantum advantage, with significant advances in QEC codes, decoding algorithms, and physical implementations. The success of QEC relies on achieving quantum gate fidelities below the error threshold of the QEC code, while accurately decoding errors through classical processing of the QEC stabilizer measurements. In this paper, we uncover the critical system-level requirements from a controller-decoder system (CDS) necessary to successfully execute the next milestone in QEC: a non-Clifford circuit. Using a representative non-Clifford circuit, of Shor’s factorization algorithm for the number 21, we convert the logical-level circuit to a QEC surface code circuit and finally to the physical level circuit. By taking into account all realistic implementation aspects using typical superconducting qubit processor parameters, we reveal a broad range of core requirements from any CDS aimed at performing error corrected quantum computation. Our findings indicate that the controller-decoder closed-loop latency must remain within tens of microseconds, achievable through parallelizing decoding tasks and ensuring fast communication between decoders and the controller. Additionally, by extending existing simulation techniques, we simulate the complete fault-tolerant factorization circuit at the physical level, demonstrating that near-term hardware performance—such as a physical error rate of 0.1% and 1000 qubits—are sufficient for the successful execution of the circuit. These results are general to any non-Clifford QEC circuit of the same scale, providing a comprehensive overview of the classical components necessary for the experimental realization of non-Clifford circuits with QEC.

Quantum error correction (QEC) currently stands as one of the most viable candidates for reaching practical quantum computation, thanks to its ability to suppress errors in quantum logic by orders of magnitude, provided the physical error rates are below a certain threshold [1,2]. As quantum hardware scales from a few qubits to hundreds, experimental demonstrations have begun to reach critical QEC milestones. These milestones range from extending the lifetimes of bosonic codes within a single optical cavity [3–7] to multi-qubit stabilizer-code demonstrations [8,9]. The stabilizer codes have shown great success in suppressing logical idle errors when increasing number of qubits [10,11], and running fault-tolerant shallow Clifford circuits [12–16].

Two classical elements of the error-corrected quantum computer affect its performance in a critical manner: (i) The controller, which executes the quantum logic, is vital in minimizing the physical gate error P_{phys} for a given quantum hardware. First, the controller's analogue pulse-generation capabilities, noise levels and stability significantly affects gate fidelity and qubit coherence times [17,18]. Second, the controller's ability to run calibrations efficiently, quickly and frequently allows continuous optimization and stabilization of the fidelities to achieve higher average fidelities over time [19–21]. (ii) The quantum error decoder, which classically processes the physical measurements of the QEC sequence to detect quantum errors. After decoding, the QEC logical error rate follows the general scaling formula [22],

$$P_{\text{log}} \propto \left(\frac{P_{\text{phys}}}{P_{\text{th}}} \right)^{\frac{d+1}{2}}, \quad (1)$$

where d is the QEC code distance and P_{th} is the QEC code error threshold. P_{th} is formally determined by the QEC code of choice, but only given accurate decoding of the quantum errors [10,23] (currently reaching $\sim 1\%$ for QEC surface code [1,22]). In recent years, a variety of approximate decoders have been explored, which while reducing P_{th} compared to the ideal decoder, may allow running the decoding task more efficiently [11,24–26]. Overall, reducing logical errors is possible by increasing the code distance (adding qubits) only if $P_{\text{phys}} < P_{\text{th}}$, taking into account the harder tasks for both the controller in reaching low average P_{phys} over the quantum processor, and the decoder in keeping a high P_{th} at scale.

Still, meeting the above requirements does not ensure a system's ability to support quantum computation. Executing non-Clifford circuits with QEC, essential for achieving quantum advantage [27], necessitates incorporating decoding-dependent quantum gates (feed-forward gates) into the circuit for each non-Clifford gate [22,28]. This introduces a new set of

requirements focused on the real-time performance of the controller, decoder, and their seamless integration. To date, the primary requirement for the decoder has been to maintain a decoding rate faster than the QEC data generation rate [29], which is the benchmark for state-of-the-art decoders [11,25,30,31] and a driving factor for QEC-focused controller architectures [32] and decoder architectures [33,34]. In a recent design [34], the authors showed how the memory requirements, the decoding latency, and the logical error rates may vary as the data to decode increases. Finally, preliminary holistic benchmarking approaches for combined controller-decoder systems (CDS) have been proposed [35]. However, a comprehensive analysis that is based on an end-to-end breakdown of a concrete circuit has been lacking, making it difficult to specify requirements and identify critical bottlenecks for the next experimental QEC milestone. In particular, gaps remain in understanding precise latency requirements — the time between the last measurement of a decoding task and its corresponding feed-forward gate operation. In addition, it is unclear what are the effects of exceeding these latency limits, what are the required real-time control-flow operations, and what are the decoding task size, number, and inter-task connectivity needed to support near-term non-Clifford circuits with QEC.

In this paper, we present an end-to-end implementation of a 5-qubit factorization circuit for the number 21 using QEC surface codes (see Figure 1a). This approach provides a detailed breakdown of the tasks that the classical CDS must handle, establishing concrete requirements for executing near-term non-Clifford circuits. Specifically, when mapping a logical circuit to a surface-level circuit that includes 12 feed-forward operations and 13 decoding tasks, we show that the decoder should handle up to 5 decoding tasks in parallel and incorporate multi-task dependencies where the result and duration of one task affect subsequent tasks. Additionally, we compile the surface-level circuit to a physical level circuit to calculate the data-flow requirements, the size of each decoding task, and the overall feed-forward latency for each decoding task, noting variations across tasks. Taking superconducting qubits as the fastest quantum computing hardware, we find that the additional error due to delayed feed-forward is not dominant if it remains within tens of microseconds throughout the circuit. While our derivation focuses on a specific example, the analysis underscores the need for advanced capabilities in quantum control systems and decoding processes, along with tighter integration between the controller and decoder and additional control-flow commands (Figure 1b). This work provides a practical set of specifications for controller-decoder systems (CDS) in near-

term fault-tolerant circuits and a foundational framework for advancing QEC towards scalable fault-tolerant quantum computation.

To reach these conclusions, we convert the original factorization circuit from the logical level to the surface code level, and ultimately to the physical level, while incorporating practical implementation considerations for realistic execution. We implement the logical circuit with native surface-codes gates given the surface connectivity constraints. These gates include fault-tolerant (FT) gates, mid-circuit feed-forward gates, and non-fault-tolerant (nFT) magic state initializations, as exemplified in Figure 1c. Each surface-level gate was then translated to its QEC physical-level circuit (example in Figure 1d) in a full physical level simulation. The end-to-end simulation results, seen in Figure 1e, show that physical errors of 0.1% and surface distance of $d = 5$ (1000 physical qubits) are sufficient for reaching meaningful logical results with total logical errors below 10%.

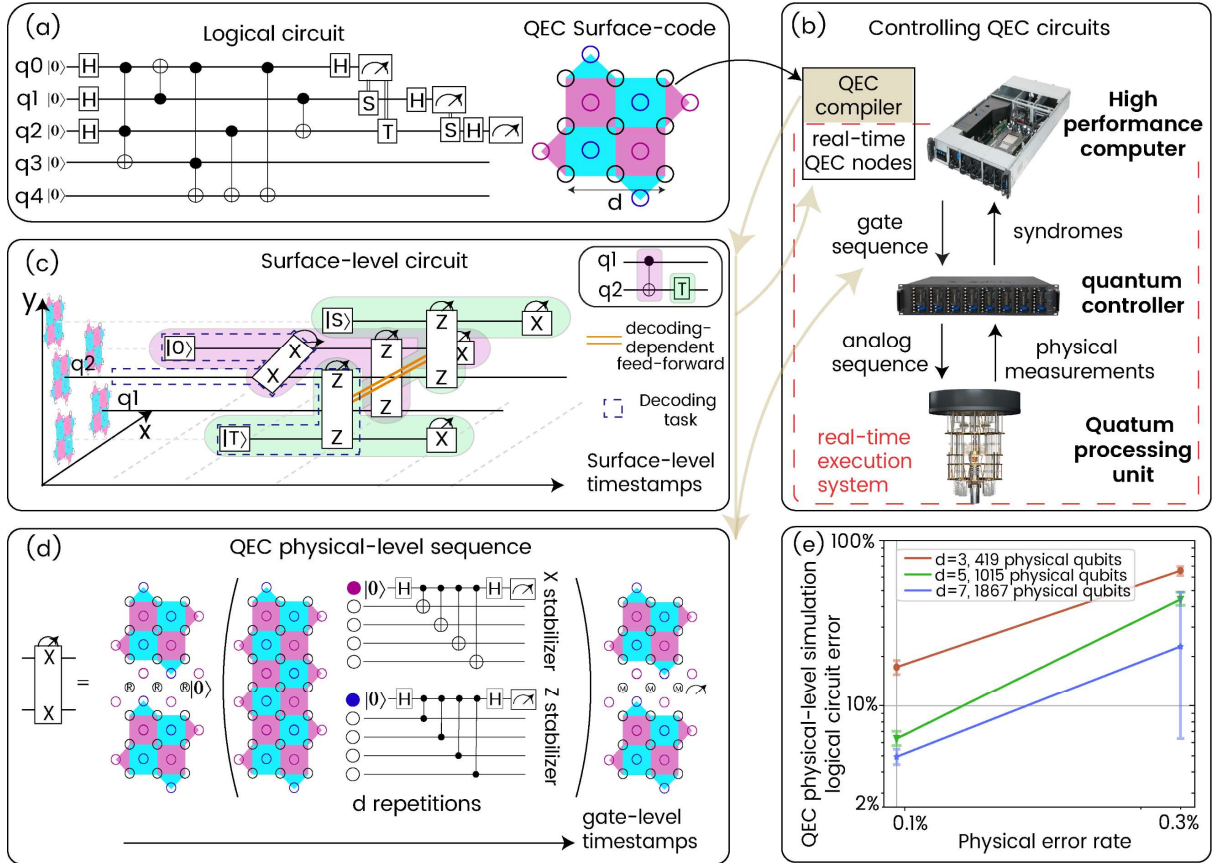


Figure 1: Overview of non-Clifford circuits with QEC, their compilation, and performance. (a) The quantum circuit used for the factorization of 21 (left). We analyze its implementation considerations with QEC surface codes (right), formed by data qubits (black circles) which encode the quantum information and ancillary qubits (blue and pink) that probe the stabilizers. (b) Schematic of the control infrastructure for QEC circuits, involving a high-performance computer (HPC) which receives the expected task and the QEC code, compiles them into a surface-level circuit, and eventually into a gate sequence (gate parameters and expected sequence) which is sent to the quantum controller. In addition, the compiler derives the expected QEC decoding tasks and sets up the required nodes. In real time (dashed red), the quantum controller applies the analog sequence to the quantum processing unit and receives physical measurements. These measurements undergo decoding which will modify subsequent circuit gate sequences. The decoding can be processed locally in the controller or using HPC nodes via a fast channel. (c) The surface-level representation of a logical CNOT (pink) and T-gate (green), implemented with 5 surfaces using FT Clifford gates and an nFT magic-state preparation ($|T\rangle$). Importantly, mid-circuit decoding-dependent feed-forward (orange) is required to implement the T-gate. For each such feed-forward operation a decoding task is needed (dashed) which include all measurements that may flip the logical result. (d) The physical-level representation of a ZZ surface-level parity check, which includes d stabilizer rounds, where is round is a circuit of depth 8. (e) Simulation results for the complete physical-level factorization circuit which implements the logical circuit with QEC surface codes quantum logic, given a specified physical error and code distance (further detailed in section III).

II. The Surface-level factorization circuit

The first step for deriving the control procedure for the factorization circuit is to convert the original logical circuit into a compatible circuit for the QEC code. For the surface code, this involves several key transformations to ensure minimal logical errors. Fault-tolerant logical gates, which reduce logical errors arbitrarily given enough physical qubits, include single-logical-qubit (i.e., single-surface) measurements and initializations in the X or Z basis, as well as multi-logical-qubit parity measurements in the Z/X basis (e.g., ZZ, XX, ZX for two surfaces) [36–39]. These gates are sufficient for implementing CNOT fault-tolerantly making it compatible for surface codes. An $|S\rangle = |0\rangle + i|1\rangle$ state can be initialized fault-tolerantly [40], enabling the S and $X^{1/2}$ gates. However, since the surface codes cannot complete a fault-tolerant universal gate set [41], a non-fault-tolerant logical initialization of a “magic-state” [42], such as $|T\rangle = |0\rangle + e^{i\pi/4}|1\rangle$ is needed for implementing the non-Clifford T gate and complete the universal gate set. Thus, to compile the original circuit to a circuit which is compatible to surface codes we modify each Toffoli (non-Clifford) gate of the original circuit into 7 T gates, initializations of magic states, CNOT gates, and S or $X^{1/2}$ gates [43] (see Figure 2a). Several methods can be used to further optimize the conversion from a general logical circuit to a surface-code compatible circuit, such as T -reduction tools [44,45] or ZX-calculus techniques [46]. This initial step is crucial since the circuit's logical error is dominated by the number of non-fault-tolerant gates.

Given a QEC-compatible circuit, the next challenge is to compile it into an exact surface-level circuit using the building blocks of the surface code (shown in Figure 2b). This conversion involves several intricate details. Firstly, maintaining fault-tolerance relies on measurement-based quantum computation. For example, each CNOT includes 3 measurements, where each measurement has a 50-50 chance of being either 0 or 1. Consequently, Pauli frames (dashed gates in Figure 2b), which are determined by the measurement result, must be tracked. Then, feed-forward (mid-circuit conditional gates) must be applied to complete each non-Clifford gate. In the T gate implementation that we use, the feed-forward is a logical S gate which is required to be applied before the next non-commuting logical gate. That is, the implementation shown in Figure 2b (right), allows delaying the feed-forward to after any commuting gate in the surface-level circuit and by that relief the requirements on the feed-forward latency (the time between the feed-forward pulse and the last measurement in depends on).

The second aspect in converting the surface-code compatible circuit to a surface-level circuit is the surface allocation. The constraints in the surface-level circuit depend on the location of each logical surface and the availability of ancillary surfaces. Typically, an $N \times N$ surface array should be sufficient for executing an N -qubit algorithm, where the computational qubits lie in a diagonal and there is a path with ancillary surfaces between each pair of qubits. The optimal allocation however is assumed to be np-hard [47] and mapping schemes are currently under development [48–50], showing linear scaling [50].

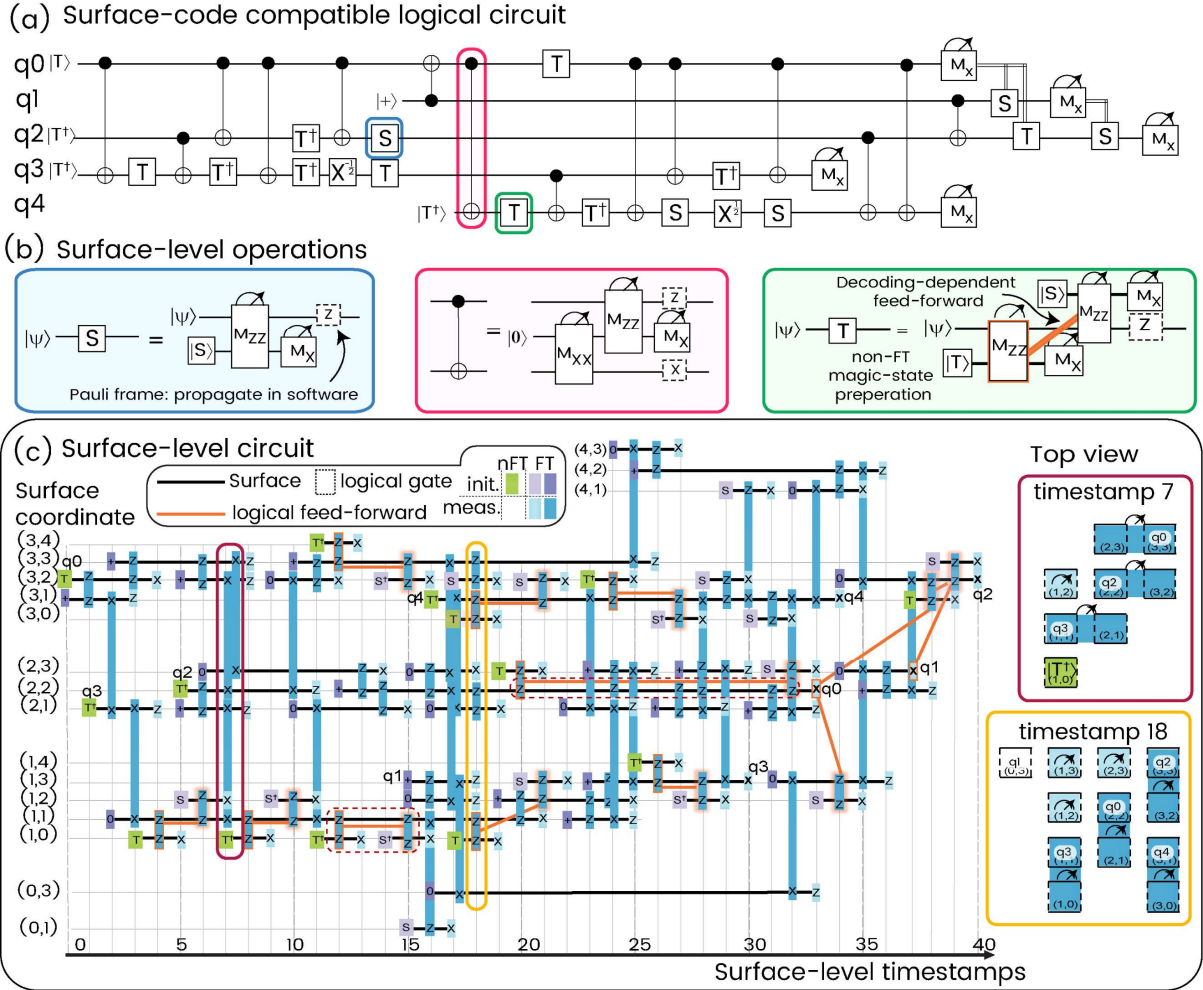


Figure 2: The steps to the surface-level factorization circuit. (a) The surface-code compatible circuit compiled from the original circuit in Fig. 1(a) to include native surface-code building-block logical operations, shown in (b). (b) The logical building-blocks for surface-code computation. These logical gates are constructed by fault-tolerant (FT) gates: initialization/measurements along the logical Pauli axes and multi-surface parity measurements in the Z/X basis. The universal gate set is made complete using the $T = \text{diag}(1, e^{\frac{i\pi}{4}})$ gate which includes a non-FT (nFT) magic-state preparation and a decoding-dependent feed-forward operation (highlighted in orange). In the T-gate implementation that we use, the feed-forward is an parity ZZ measurement with a prepared $|S\rangle$ state which can be delayed until the next non-commuting gate in the circuit. (c) The surface-level circuit which implements the circuit from (b) using 18 surfaces. This implementation was done manually and can be further optimized to minimize either the number of surfaces, the circuit depth, or ease the feed-forward latency requirements. Notably, in most cases, the feed-forward operations do not need to be executed immediately after their corresponding logical measurement either because they can be delayed by commuting them with following gates (dashed, timesteps 20-31, surface (2,2)) or due to idle times needed until availability of an ancillary qubit (dashed, timesteps 12-15, surface (1,1)). Insets: a top view of surface-level timestamp 7 (top) and 18 (bottom), including the logical gate of each surface, surface coordinate, and indication of the corresponding logical qubit.

The complete surface-level factorization circuit with native surface-code logical gates is depicted in Figure 2c, using 18 surfaces and 40 surface-level timestamps. A timestamp comprises d stabilizer rounds (as illustrated in Figure 1d) with the quantum logic operations occurring before (initializations), after (single-surface measurement), or during (parity measurements) these d rounds. The five computational qubits are initialized during the circuit and remain active, either by idling or teleportation, until their logical measurement (their initializations and measurements are noted in Figure 2c). For executing the correct quantum logic under the topology constraints, we added 13 ancillary surfaces which enable the necessary T gates and logical CNOT gates. Figure 2c inset presents the locations of the logical surfaces in timestamps 7 and 18. Further optimizations can be made on this circuit, such as minimizing circuit depth or ease the feed-forward latency demands (horizontal length of orange lines in Figure 2c). Importantly, the feed-forward latency demands are relieved (1) by propagating the feed-forward operation through the circuit until the next non-commuting gate dashed, timesteps 20-31, surface (2,2)) or (2) due to the idling time when logical surfaces are waiting for an available ancillary qubit (dashed, timesteps 12-15, surface (1,1)). In addition, reducing the number of surfaces is clearly possible but at the expense of extended circuit depth since the surfaces in coordinates (3,4) and (0,1) are used for only 3 timestamps. Table 1 presents various parameters of the surface-level circuit from which we derive the control requirements.

<i>Parameter</i>	<i>Size</i>
Total surfaces used	18
Average number of active surfaces	7.5
Total measurements	105
Feed-forward gates	13
Average Fault-tolerant gates (including idling)	296
Average Non-fault-tolerant blocks	13.5
Decoding tasks	13
Average feed-forward latency [d rounds]	2.1

Table 1: Summary of the surface-level circuit parameters according to the implementation in Figure 2c.

With the surface-level circuit established, we can estimate the fidelity requirements for the physical qubits. The error budget is estimated by categorizing the gates into nFT gates which are the magic-state initializations (green in Figure 2c), and FT gates, which include idling, initializations, measurements in the Pauli basis, and parity measurements in the Z/X basis. All FT gates exhibit error reduction when increasing the distance, and the error rates for all single-surface-level timestamp are similar (d stabilizer rounds for a single surface, e.g., a d^3 block), though the two-qubit parity gate and the $|S\rangle$ initializations (or measurement in the Y basis for

other S gate implementations [40]) contribute to the total error as 2 FT gates. Thus, by counting the total number of FT gates and the number of nFT initializations, it is straightforward to estimate the expected error of the whole circuit. To obtain the errors of the basic QEC operations, we simulate the logical errors of two simple circuits: idling a single surface in Z/X basis of distance d for d stabilizer rounds, shown in Figure 3a, and a nFT magic state initialization (we used the hook-injection technique [51]), shown in Figure 3b. In these small-scale simulations, and in large-scale simulations (in section III), the physical error model includes a rate of p_{phys} for depolarizing any 2-qubit gate and flipping a physical measurement, while the single qubit gate error was $p_{\text{phys}}/10$. In addition, we included post-selection (PS) that we applied within the nFT initialization procedure, keeping cases with only ‘0’ stabilizer measurements during the surface expansion [51] which reduces by a factor of 3 the initialization error.

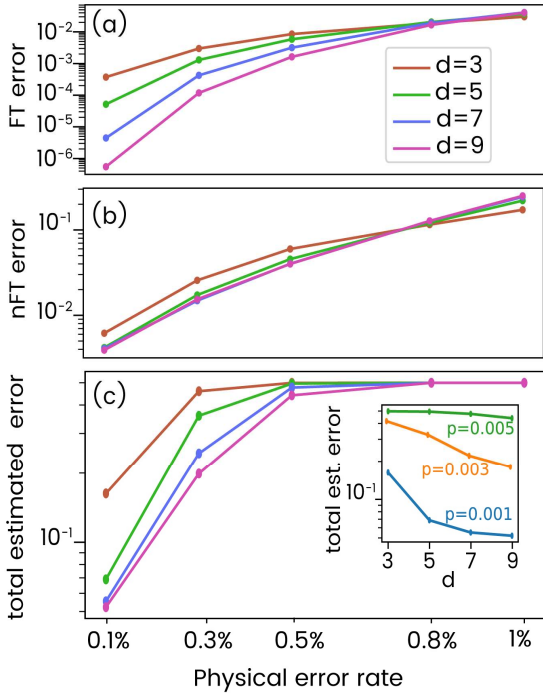


Figure 3: Error estimation for the factorization circuit. (a) Single FT error, e.g., the logical error in idling d stabilizer rounds. (b) nFT preparations error. Increasing the code’s distance does not reduce the logical error. (c) The estimated error of the factorization circuit calculated (binomially) as the probability for an odd number of flips in 14 nFT gates and 296 FT gates. Inset: The estimated error of the factorization circuit as a function of distance, showing saturation to $\sim 5\%$. From this estimation, successfully running ($>90\%$ fidelity) this circuit would require a physical error of 0.1% and $d \geq 5$.

Figure 3c presents the total estimated error of the factorization circuit, calculated from the error outcome from the two small-scale simulations. We find that a physical error rate of 0.1% and $d \geq 5$ is expected to be required to reach an acceptable fidelity of above 90% (see SM section S2) while a physical error rate of 0.3% is expected to be too high. This estimation shows that the nFT initializations dominate the error budget for $d \geq 5$ when $P_{\text{phys}} = 0.1\%$ which creates a fidelity saturation when increasing the distance (see Figure 3c inset). Thus, we find that in these circuits the nFT initialization fidelity practically determines the number of non-Clifford

gates for any QEC circuit, emphasizing that the control requirements on fidelity relates to the number of non-Clifford gates in the logical circuit. The dominance of the nFT magic state initialization error compared to other logical gates underscores the unique error sources in QEC circuits. In non-QEC circuits, Clifford and non-Clifford single-qubit gates are on equal footing, whereas entangling gates and measurements are significantly more error-prone. This understanding drives the development of low-error magic-state initialization techniques, as was recently suggested by Gidney [52].

III. Physical-level simulations

To verify the required fidelities and derive the physical-level control aspects of the factorization circuit, we simulated an end-to-end physical circuit that implements the surface QEC codes for the logical circuit depicted in Figure 4a, involving thousands of qubits. This simulation was conducted using the stim Python package [53], which facilitates the simulation of noisy quantum circuits at large scale, maps the circuits to a decoding task, and performs full decoding to verify that the physical pulse-sequence is indeed fault-tolerant (or exhibits minimal error for the nFT initializations). We extended the basic package infrastructure to enable the coding of the surface-level circuit in a logical & surface-level intermediate representation, so that the complete physical-level sequences are automatically compiled (see SM section S1). However, the simulation does not include two features of the factorization circuit: decoding-dependent mid-circuit gate modification and non-Clifford gates as the stim package only supports stabilizer states. To approximate the factorization circuit under these constraints, we removed feed-forward gates from the circuit in Figure 2a and substituted the non-Clifford T gates and $|T\rangle$ initializations with S gates and $|S\rangle$ initializations, respectively, which we implemented non-fault tolerantly. This involved replacing a single physical-level $X^{1/4}$ gate with \sqrt{X} for each nFT initialization of the $|S\rangle$ states that replaced the $|T\rangle$ magic states. The simulation enabled a verification of the physical gate sequence that keeps fault-tolerance with tens of surfaces and thousands of physical qubits. We verified correctness of the logic through 3 out of 5 logical stabilizers ($X_{q_0}X_{q_4}, X_{q_1}X_{q_2}, X_{q_3}$) which we defined as the simulation observables to the circuit from Figure 4a.

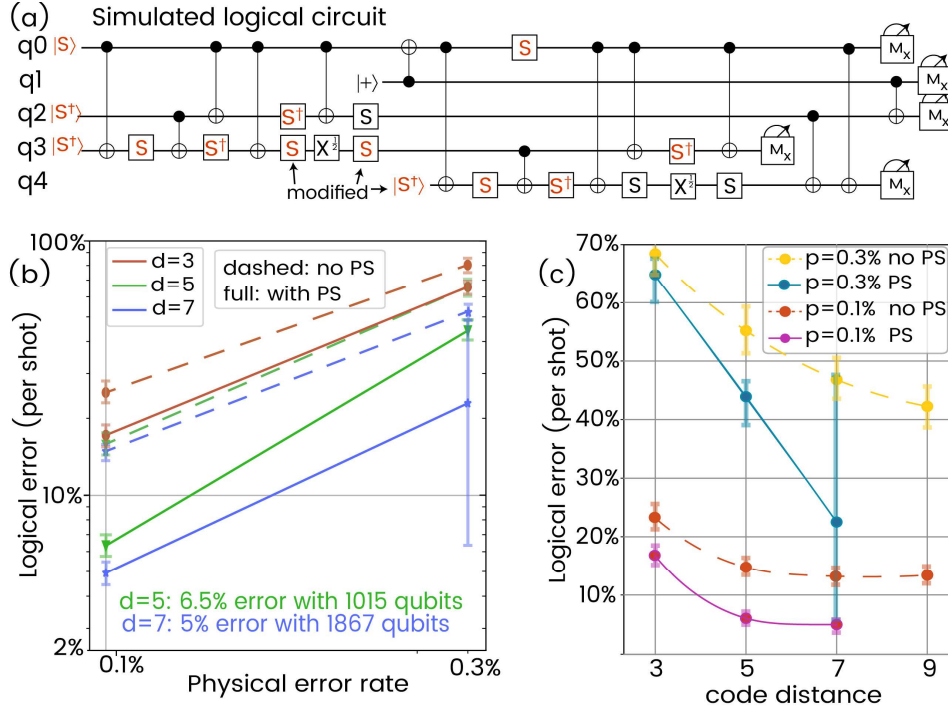


Figure 4: Simulation of the factorization circuit. (a) The simulated logical circuit, which mirrors the circuit in Figure 1b, with T gates converted to S gates (implemented non-fault-tolerantly). Modified operations are marked red. The simulated physical-level implementation of this logical circuit did not include feed-forward operations. **(b)** The logical error of the simulated factorization circuit vs physical error with and without post-selection (PS). Due to nFT initializations, the gain in $d = 7$ is negligible compared to the $d = 5$ circuit for physical errors of 0.1% and reaching meaningful results for the factorization circuit (90% logical fidelity) is beyond reach with physical errors of 0.3%. The error bars correspond to a 99.9% confidence in a binomial fit. **(c)** The logical error vs the code distance, showing the logical error saturation when increasing the distance due to the dominance of the nFT initializations.

Our simulations implemented all single and two-qubit logical gates within the Z/X basis fault-tolerantly at the physical level and included $|S\rangle$ (or $|\sqrt{X}\rangle = |+\rangle + i|-\rangle$) initializations using state hook injection [51] with the distance and physical error probability as free parameters. The simulation also mapped physical measurements to a decoding graph to enable the complete decoding and eventually extract the QEC logical error of the whole circuit. Detailed implementation is provided in Supplementary Materials section S1 and Figure S1. Briefly, each surface is defined by its coordinate in a two-dimensional grid, its distance, and its orientation (which edges correspond to the logical Z and X), while the surface operations are translated to the physical implementation for each physical-level timestamp within a surface-level operation. Examples include initializing ancillary qubits in the first stabilizer round timestamp, data qubit initializations or measurements when initializing or measuring any single surface,

or lattice surgery initialization or termination. These physical gates are then invoked when defining a specific surface-level gate (such as the gate sequence from Figure 2c). Importantly, we retain parts of the original logical-level circuit information, such as the location of the logical qubits and the logical timestamp within the logical circuit, which is crucial for tracking logical Pauli frames from each logical measurement. The full physical-level gate sequences for distance 3 is shown in SM video 1.

Figures 4b and 4c illustrate the logical errors of the simulated circuit given the surface distance, physical errors of 0.1% and 0.3%, and with or without post-selection (PS) during the nFT initializations. The PS was on the nFT state initializations with ‘0’ values for all syndromes during the state injections process when expanding the surface from $d = 2$ to the required surface distance. The results align with the anticipated error summation technique from Figure 3, indicating that the circuit fidelity will not exceed 90% for a physical error of 0.3%, even with PS and $d = 7$. We also observe the expected saturation of logical error at $\sim 5\%$ for $d \geq 5$ with PS. Consequently, 1000 physical qubits are sufficient to run non-Clifford circuits with QEC with approximately 15 non-Clifford gates while increasing beyond 1000 qubits does not significantly improve logical fidelity when the physical error rate is 0.1%. An advantage in increasing the distance can be reached only by reducing the nFT initialization error. Thus, QEC circuits that go beyond a thousand qubits should focus on magic-state distillation [38,54,55], and in any case center efforts on reducing nFT initialization errors.

Table 2 presents resource estimates which we extract from the physical level analysis of the factorization circuit above and are relevant for the future designs of QEC circuits and QEC control systems. In the first column, we address the required size of the quantum chip, which is a few hundreds to few thousands of physical qubits. Another critical resource metric is the number of simultaneous control channels required to perform the physical gates. While single qubit gates need to be performed on all active qubits in parallel, meaning that the number of single qubit control channels is expected to equal to the total number of qubits, analysis of our implementation shown in column 2 reveals that not all qubits are controlled in parallel (55%-65%), allowing us to benefit from multiplexed control. The same is true for two-qubit gates and readout, as shown in columns 3 and 4 respectively. We next discuss classical processing resource requirements. The control system must convert thousands of analog physical measurements to digital data in each run and subsequently decode the data. The average data creation rate is a critical factor which determines the data transfer between the controller and the decoder in a CDS, defining the channel bandwidth measured in bits per second. When

considering a stabilizer round with duration of 1 microsecond (as in superconducting qubits [10]), bandwidths of $\frac{1 \text{ Mbi}}{\text{sec}} \times \text{qubits}$ will be sufficient to transfer all measurement data. Finally, we note that the run of the whole circuit will take less than a millisecond for superconducting qubits, since the total number of stabilizer rounds scales only as d .

	#physical qubits	max active qubits	max parallel 2-Q gate	max parallel measurements	#physical measurements	Avg data creation rate [bit per QEC round]	Total stabilizer rounds
scale	d^2	d^2	d^2	d^2	d^3	d^2	d
$d = 3$	419	232	88	112	8061	69	117
$d = 5$	1015	632	268	312	36687	188	195
$d = 7$	1867	1224	544	608	96006	363	273
$d = 9$	2975	2008	916	1000	203874	595	351

Table 2: Physical-level implementation aspect, as extracted from simulations.

IV. Decoding resource requirements for non-Clifford circuits

Fulfilling the potential of QEC and achieving the logical error reduction to the QEC quantum computation as described in Eq. 1 relies on the CDS’s ability to apply mid-circuit, decoding-dependent gates with low latency. Here we define latency as the time interval between the last measurement of a decoding task and the mid-circuit quantum operation that depends on it. The decoder, a classical processor, detects local quantum errors based on the physical QEC measurement results, as well as an error model associated with control operations. The field of decoding algorithms is rapidly advancing, with solutions exhibiting tradeoffs between accuracy, decoding time, and classical resources [24,26,31,56–60]. While the Clifford QEC circuits demonstrated experimentally so far allow for post-processing decoding, non-Clifford gates require real-time decoding-dependent feed-forward. Recent works had shown that control system latency determines the success in implementing large-scale non-Clifford circuits [34,35], motivating the focus on analyzing a CDS as the controller and decoder must be tightly connected. Ref. [35] also introduced the first holistic benchmarks for evaluating CDS based on low-latency feed-forward operations. In this chapter, we analyze for the first time the expected decoding task size and requirements, based on an expected near-term use-case.

Figure 5a presents the 13 different decoding tasks of the factorization circuit, where each highlighted color represents a separate, self-contained decoding task. Each decoding task ends

with a logical measurement that determines, unless the circuit ends, a decoding-dependent mid-circuit conditional gate according to the decoding result. This result is sent to the controller to apply the gate, but it is also sent to subsequent decoding tasks, as the result also influences the dimensions of subsequent decoding tasks, i.e., the number of physical measurements to be analyzed and the connectivity between them. All decoding tasks may potentially start in the beginning of the circuit and include all measurements until the last measurement which will affect the corresponding feed-forward. However, we suggest avoiding decoding redundancy by communicating boundary conditions and logical Pauli frame flips between decoding tasks so that there is a minimal overlap between decoding tasks. The frame updates should be transferred before the feed-forward gate of the receiving task. Figure 4b shows these dependencies and the active time of each task. It is evident that non-Clifford circuits require the decoding unit to execute multiple decoding tasks in parallel (up to four in this case) and facilitate communication between the tasks to update Pauli frames and task shapes. We note that in our T gate implementation, the shape-dependencies must be communicated between decoders, though this information can be converted to frame-dependencies in other implementations [38]. These requirements highlight the need for a new perspective: from a single decoder handling the entire QEC experiment to a decoding unit which processes different tasks in parallel with dependencies between them.

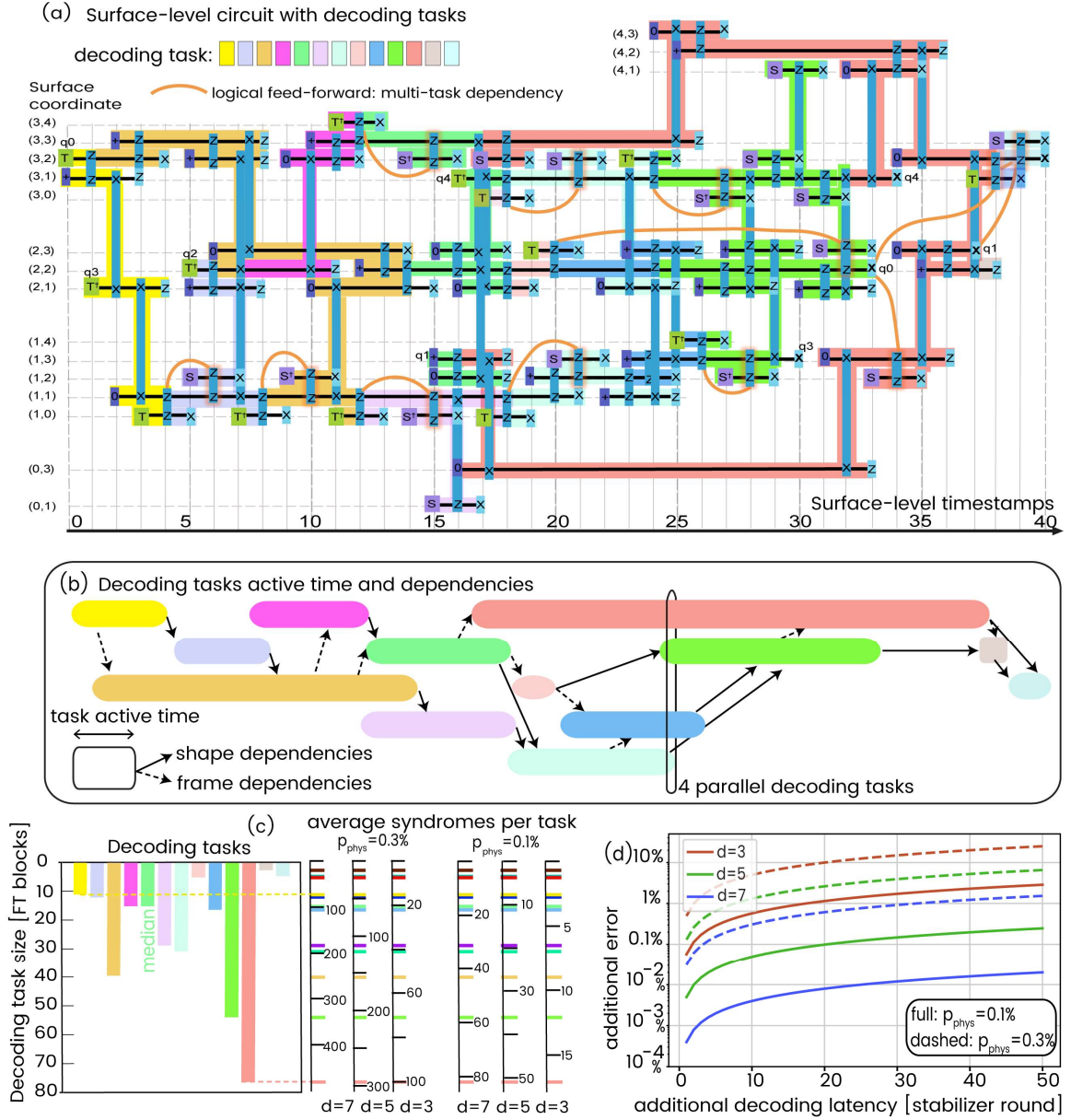


Figure 5: Decoding aspects of shallow non-Clifford circuits. (a) The surface-level circuit from Figure 1d, including the different 13 decoding tasks with color-coding. (b) The active time of each decoding task and the shape or frame dependencies between the decoding tasks (arrows). We find that the decoder should be able to solve ~ 5 decoding tasks in parallel, and decoding tasks are strictly interdependent by shape (full arrows). The decoding unit is also required to transfer Pauli frames of surfaces between one another (dashed arrows). (c) The size of each decoding task (left), and the average syndromes per task (right) given specific distance and physical error rate, marked here as separate axes for each error rate and distance. The horizontal lines for each axis correspond to the bars on the left and serve as a guide to the eye. The low average syndrome rate per task, for some tasks, motivates the importance of a local pre-decoding stage within the controller [61]. (d) The additional error to the whole circuit due to a delay in the decoding latency, showing how a large distance and low error rate can relax the requirements of the decoding latency. For example, every 20 rounds of delay when $p_{\text{phys}}=0.1\%$ and $d = 5$ will add only 0.1% for the overall circuit error.

To further estimate the requirements on the decoding unit, we provide an estimation of the average number of detected syndromes (either a physical error or a measurement error) within each decoding task. We estimate the expected number of measured syndromes, which indicates the classical processing load, for each decoding task. The estimation is based on the space-time volume of the task, defined as the number of FT blocks (d stabilizer rounds for a distance- d surface). Figure 4c presents the space-time volume of each decoding task in the factorization circuit, and the corresponding average number of syndromes for different distances and physical error rates (right scales). We find that for a low distance ($d = 3$) and low error rates (0.1%), most of the tasks have fewer than five syndromes on average. These low number of syndromes motivates the development of an embedded decoder within the controller, for example with an FPGA decoding scheme [25], as suggested in various micro-architecture schemes [33]. Additionally, a pre-decoder stage, as recently proposed [61,62], could potentially resolve a significant proportion of the syndromes, leaving only the remaining syndromes to be handled by fast and dedicated decoding hardware (such as in [30,33,63]).

The additional logical error due to a delay in the decoding-dependent feed-forward latency for different distances and physical error rates is presented in Figure 5d. This error is calculated using the equation $P_{delay} = N \cdot P_{FT} \frac{T_{delay}}{d \cdot T_{round}}$, where T_{delay} is the delay in the feed-forward latency, T_{round} is the time of a single stabilizer round, and P_{FT} is a single FT error per d rounds for a single surface. N refers to the number of logical qubits in the original logical circuit (five in this case) which must remain idle until the feed-forward is applied. The calculation of P_{delay} in our system shows that if the sum of T_{delay} for all decoding tasks of the circuit is below tens of μs , the additional error remains insignificant compared to the nFT gate error. Importantly, magic-state distillation schemes have a similar number of nFT gates (e.g., 15-to-1 scheme) as our circuit. Consequently, our result also defines the latency requirements for the magic-state distillation circuit to enable qubit-efficient distillation schemes [38].

V. Summary and Discussion

Throughout this manuscript, we have analyzed various aspects of the control system for successfully executing a non-Clifford circuit with QEC. Figure 6 summarizes our findings, categorizing the requirements into those of the controller, the decoder, and their communication channel. Regarding the controller, we emphasize the need for low coherent

control errors. Specifically, the physical error rate should be kept below 0.1% for 1000 qubits and approximately 0.3% for few thousands of qubits if logical error demands can be relieved. Additionally, it is necessary for the CDS to support conditional gate execution for the real-time feed-forward operations. To ensure low-latency feed-forward, it is necessary to have an ultra-low QPU-controller latency and a pre-decoding classical processing stage to alleviate the requirements on the decoder-controller communication channel and the decoder throughput requirements, thereby achieving higher overall fidelity.

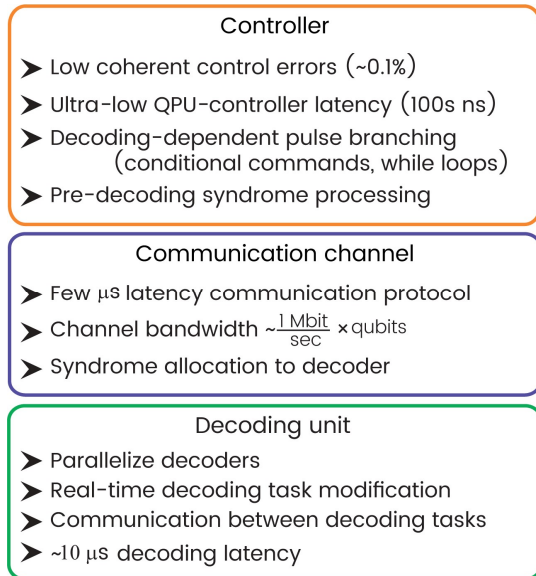


Figure 6: The controller-decoder system requirements for running non-Clifford circuits in QEC. The controller must be able to execute the optimized sequence, with low latency with the QPU, as well as local classical operations such as classical branching and pre-decoding. The communication channel should run on a fast link with high enough bandwidth to send all syndromes to the decoder. The decoder should be able to run several decoding tasks in parallel while knowing the dependencies between the decoders.

Supporting low-latency decoding-dependent feed-forward operations is the primary rationale behind the requirements for the communication channel and the decoding unit. Assuming a worst-case scenario with quantum hardware requiring a microsecond for a stabilizer round, as in superconducting transmon qubits, the total two-way communication and decoding latency must remain within tens of microseconds. This time budget should be allocated primarily to the decoder to maximize decoding time, leaving the communication channel with a latency timescale of a few microseconds. The communication channel should support a bandwidth of around Mbit/sec for each active qubit if all syndromes are transmitted (1 bit per physical qubit per stabilizer round). However, this requirement can be reduced with a pre-processing stage to transmit only the detected syndromes. Finally, maintaining low latency necessitates that the decoding unit can execute multiple decoding tasks in parallel, facilitate communication between tasks, and dynamically modify the shape of the decoding tasks in real-time.

Although these requirements were derived from a specific circuit, they can be considered as guidelines to every non-Clifford circuit with a few thousand physical qubits and ~ 15 nFT gates

such as the well-known 15-to-1 magic state distillation procedures. In all such circuits, the overall fidelity is determined by the fidelities of the nFT and FT gates and their total count throughout the circuit. We anticipate that the nFT fidelity will limit the number of non-Clifford gates to few tens, as Clifford circuits can be minimized using ZX calculus. This number of non-Clifford gates dictates the number of required decoding tasks. We do not expect significant deviations in the size of decoding tasks because any non-Clifford circuit will follow a similar pattern of entangling surfaces and applying non-Clifford gates between the entanglement operations. The number of surfaces will be constrained by the total number of qubits which can hold sufficiently low physical error rates. This constraint will also set a limit on the overall controller-decoder communication requirements. Notably, these requirements are independent of the decoding algorithm or the specific variant of the surface code used (for example, the ZXXZ code).

This paper highlights several bottlenecks in the experimental execution of non-Clifford circuits, emphasizing the need for advancements in QEC research. Addressing the circuit fidelity bottleneck can involve improving techniques for reducing errors in nFT magic-state initializations [52,64], or developing small-scale distillation methods [52]. Additionally, scalable qubit characterization techniques [65], [66] or error learning [62] are essential for minimizing the physical error rate, which may be facilitated by the fact that only specific physical gates are required. From an algorithmic perspective, developing a compiler that transforms a logical circuit to a surface-level circuit, considering qubit topology constraints, would be highly beneficial. Moreover, it is crucial to find ways to decode lattice surgery during circuit execution, enable decoding-dependent mid-circuit operations (a limitation of the simulation within this paper), and enable communication between decoders. On the hardware front, further development of efficient controller-decoder connectivity is necessary to support the latency and decoder connectivity requirements presented in this paper.

Our conceptual results can be extrapolated to larger quantum algorithms. For example, all requirements in Figure 6 will stand for a factorization of a larger number. However, the number of required non-Clifford gates will force the need for magic-state distillation schemes, in addition to routing the magic states to the computational surface (which was found to be dominant in resource estimation [67]). Therefore, the scaling of the physical resources per logical qubit in the original quantum circuit will significantly grow when adding a magic-state distillation procedure as part of the algorithm. To enable further scaling, it is important to

develop computational techniques for quantum LDPC codes [68], which rely on at least two planar quantum hardware layers [69]. Recent proposals suggest that such a 3D architecture could enable computation with a cat-LDPC code [70], potentially overcoming the high surface connectivity overhead we identified (18 surfaces for a 5-qubit algorithm). In all these cases, the control requirements are expected to follow similar guidelines, as the computation is measurement-based and necessitates real-time decoding.

In conclusion, this paper presents a comprehensive outline of the requirements and considerations necessary for running fault-tolerant quantum algorithms, specifically focusing on non-Clifford circuits. By detailing the control system requirements, decoding dependencies, and fidelity constraints, we have laid the groundwork for the successful implementation of these advanced quantum algorithms. This work is a crucial step toward the realization of fault-tolerant quantum computation and sets the stage for experimental demonstrations of non-Clifford circuits in the near term. As quantum hardware progresses to support a few hundred to thousands of qubits, the insights provided here will guide the development of the CDS which plays a critical role in the scaling of quantum supercomputers [71], ultimately enabling the execution of complex quantum algorithms with high fidelity. Implementing the suggested guidelines in real hardware will mark a significant milestone in the journey towards scalable, error-corrected quantum computation.

References

- [1] E. Dennis, A. Kitaev, A. Landahl, and J. Preskill, "Topological quantum memory," *J. Math. Phys.* **43**, 4452 (2002).
- [2] E. Knill, R. Laflamme, and W. H. Zurek, "Resilient Quantum Computation: Error Models and Thresholds," *Proc. R. Soc. Lond. Ser. Math. Phys. Eng. Sci.* **454**, 365 (1998).
- [3] N. Ofek *et al.*, "Extending the lifetime of a quantum bit with error correction in superconducting circuits," *Nature* **536**, 441 (2016).
- [4] V. V. Sivak *et al.*, "Real-time quantum error correction beyond break-even," *Nature* **616**, 50 (2023).
- [5] M. Puviani, S. Borah, R. Zen, J. Olle, and F. Marquardt, "Boosting the Gottesman-Kitaev-Preskill Quantum Error Correction with Non-Markovian Feedback," arXiv:2312.07391.
- [6] D. Lachance-Quirion *et al.*, "Autonomous Quantum Error Correction of Gottesman-Kitaev-Preskill States," *Phys. Rev. Lett.* **132**, 150607 (2024).
- [7] U. Réglade *et al.*, "Quantum control of a cat-qubit with bit-flip times exceeding ten seconds," *Nature* **629**, 778 (2024).
- [8] J. Kelly *et al.*, "State preservation by repetitive error detection in a superconducting quantum circuit," *Nature* **519**, 66 (2015).
- [9] S. Krinner *et al.*, "Realizing Repeated Quantum Error Correction in a Distance-Three Surface Code," *Nature* **605**, 669 (2022).
- [10] Google Quantum AI *et al.*, "Suppressing quantum errors by scaling a surface code logical qubit," *Nature* **614**, 676 (2023).
- [11] R. Acharya *et al.*, "Quantum Error Correction below the Surface Code Threshold," arXiv:2408.13687.
- [12] D. Bluvstein *et al.*, "Logical quantum processor based on reconfigurable atom arrays," *Nature* **626**, 58 (2023).
- [13] C. Ryan-Anderson *et al.*, "High-Fidelity and Fault-Tolerant Teleportation of a Logical Qubit Using Transversal Gates and Lattice Surgery on a Trapped-Ion Quantum Computer," arXiv:2404.16728.
- [14] B. Hetényi and J. R. Wootton, "Creating Entangled Logical Qubits in the Heavy-Hex Lattice with Topological Codes," arXiv:2404.15989.
- [15] M. P. da Silva *et al.*, "Demonstration of Logical Qubits and Repeated Error Correction with Better-than-Physical Error Rates," arXiv:2404.02280.
- [16] B. W. Reichardt *et al.*, "Demonstration of Quantum Computation and Error Correction with a Tesseract Code," arXiv:2409.04628.
- [17] A. Vepsäläinen *et al.*, "Improving qubit coherence using closed-loop feedback," *Nat. Commun.* **13**, 1932 (2022).
- [18] P. V. Klimov, J. Kelly, J. M. Martinis, and H. Neven, "The Snake Optimizer for Learning Quantum Processor Control Parameters," arXiv:2006.04594.
- [19] J. Kelly *et al.*, "Scalable in-situ qubit calibration during repetitive error detection," *Phys. Rev. A* **94**, 032321 (2016).
- [20] Y. Xu *et al.*, "Automatic Qubit Characterization and Gate Optimization with QubiC," *ACM Trans. Quantum Comput.* **4**, 1 (2023).
- [21] T. Proctor *et al.*, "Detecting and tracking drift in quantum information processors," *Nat. Commun.* **11**, 5396 (2020).
- [22] A. G. Fowler, M. Mariantoni, J. M. Martinis, and A. N. Cleland, "Surface codes: Towards practical large-scale quantum computation," *Phys. Rev. A* **86**, 032324 (2012).
- [23] A. deMarti iOlius, P. Fuentes, R. Orús, P. M. Crespo, and J. E. Martinez, "Decoding Algorithms for Surface Codes," *Quantum* **8**, 1498 (2024).
- [24] N. Delfosse and N. H. Nickerson, "Almost-linear time decoding algorithm for topological codes," *Quantum* **5**, 595 (2021).
- [25] N. Liyanage *et al.*, "Scalable Quantum Error Correction for Surface Codes Using FPGA," in *2023 IEEE International Conference on Quantum Computing and Engineering (QCE)* **1**, 916 (2023).
- [26] Y. Wu and L. Zhong, "Fusion Blossom: Fast MWPM Decoders for QEC," in *2023 IEEE International Conference on Quantum Computing and Engineering (QCE)* **1**, 928 (2023).

- [27] D. Gottesman, "The Heisenberg Representation of Quantum Computers," arXiv:quant-ph/9807006.
- [28] P. O. Boykin *et al.*, "On universal and fault-tolerant quantum computing: a novel basis and a new constructive proof of universality for Shor's basis," in *Proceedings of the 40th Annual Symposium on Foundations of Computer Science*, FOCS '99 (IEEE Computer Society, Washington, DC, 1999), p. 486.
- [29] B. M. Terhal, "Quantum Error Correction for Quantum Memories," *Rev. Mod. Phys.* **87**, 307 (2015).
- [30] B. Barber *et al.*, "A Real-Time, Scalable, Fast and Highly Resource Efficient Decoder for a Quantum Computer," arXiv:2309.05558.
- [31] F. Battistel *et al.*, "Real-time decoding for fault-tolerant quantum computing: progress, challenges and outlook," *Nano Futur.* **7**, 032003 (2023).
- [32] X. Fu *et al.*, "A control microarchitecture for fault-tolerant quantum computing," *Microprocess. Microsyst.* **70**, 21 (2019).
- [33] P. Das *et al.*, "AFS: Accurate, Fast, and Scalable Error-Decoding for Fault-Tolerant Quantum Computers," in *2022 IEEE International Symposium on High-Performance Computer Architecture (HPCA)* (IEEE, Seoul, Korea, Republic Of, 2022), pp. 259–273.
- [34] S. Maurya and S. Tannu, "Managing Classical Processing Requirements for Quantum Error Correction," arXiv:2406.17995.
- [35] Y. Kurman *et al.*, "Benchmarking the ability of a controller to execute quantum error corrected non-Clifford circuits," arXiv: 2311.07121.
- [36] D. Horsman *et al.*, "Surface code quantum computing by lattice surgery," *New J. Phys.* **14**, 123011 (2012).
- [37] C. Chamberland and E. T. Campbell, "Universal Quantum Computing with Twist-Free and Temporally Encoded Lattice Surgery," *PRX Quantum* **3**, 010331 (2022).
- [38] D. Litinski, "A Game of Surface Codes: Large-Scale Quantum Computing with Lattice Surgery," *Quantum* **3**, 128 (2019).
- [39] O. Higgott *et al.*, "Improved Decoding of Circuit Noise and Fragile Boundaries of Tailored Surface Codes," *Phys. Rev. X* **13**, 031007 (2023).
- [40] C. Gidney, "Inplace Access to the Surface Code Y Basis," *Quantum* **8**, 1310 (2024).
- [41] B. Eastin and E. Knill, "Restrictions on Transversal Encoded Quantum Gate Sets," *Phys. Rev. Lett.* **102**, 110502 (2009).
- [42] S. Bravyi and A. Kitaev, "Universal Quantum Computation with ideal Clifford gates and noisy ancillas," *Phys. Rev. A* **71**, 022316 (2005).
- [43] M. Amy, D. Maslov, M. Mosca, and M. Roetteler, "A meet-in-the-middle algorithm for fast synthesis of depth-optimal quantum circuits," *IEEE Trans. Comput.-Aided Des. Integr. Circuits Syst.* **32**, 818 (2013).
- [44] A. Kissinger and J. Van De Wetering, "Reducing the number of non-Clifford gates in quantum circuits," *Phys. Rev. A* **102**, 022406 (2020).
- [45] N. De Beaudrap, X. Bian, and Q. Wang, "Techniques to Reduce $\pi/4$ -Parity-Phase Circuits, Motivated by the ZX Calculus," *Electron. Proc. Theor. Comput. Sci.* **318**, 131 (2020).
- [46] B. Coecke, "Basic ZX-Calculus for Students and Professionals," arXiv:2303.03163.
- [47] D. Herr, F. Nori, and S. J. Devitt, "Optimization of lattice surgery is NP-hard," *npj Quantum Inf.* **3**, 35 (2017).
- [48] L. Lao *et al.*, "Mapping of Lattice Surgery-based Quantum Circuits on Surface Code Architectures," *Quantum Sci. Technol.* **4**, 015005 (2018).
- [49] M. Beverland, V. Kliuchnikov, and E. Schoute, "Surface Code Compilation via Edge-Disjoint Paths," *PRX Quantum* **3**, 020342 (2022).
- [50] Y. Akahoshi *et al.*, "Partially Fault-tolerant Quantum Computing Architecture with Error-corrected Clifford Gates and Space-time Efficient Analog Rotations," *PRX Quantum* **5**, 010337 (2024).
- [51] C. Gidney, "Cleaner Magic States with Hook Injection," arXiv:2302.12292.
- [52] C. Gidney, N. Shutty, and C. Jones, "Magic State Cultivation: Growing T States as Cheap as CNOT Gates," arXiv:2409.17595.
- [53] C. Gidney, "Stim: a fast stabilizer circuit simulator," *Quantum* **5**, 497 (2021).

- [54] J. Haah and M. B. Hastings, "Codes and Protocols for Distilling TTT, controlled-SSS, and Toffoli Gates," *Quantum* **2**, 71 (2018).
- [55] D. Litinski, "Magic State Distillation: Not as Costly as You Think," *Quantum* **3**, 205 (2019).
- [56] V. Kolmogorov, "Blossom V: a new implementation of a minimum cost perfect matching algorithm," *Math. Program. Comput.* **1**, 43 (2009).
- [57] C. T. Chubb, "General Tensor Network Decoding of 2D Pauli Codes," arXiv:2101.04125.
- [58] P. Das, A. Locharla, and C. Jones, "LILLIPUT: A Lightweight Low-Latency Lookup-Table Based Decoder for Near-Term Quantum Error Correction," in *Proceedings of the 27th ACM International Conference on Architectural Support for Programming Languages and Operating Systems*, 541 (2022)
- [59] K. Meinerz, C.-Y. Park, and S. Trebst, "Scalable Neural Decoder for Topological Surface Codes," *Phys. Rev. Lett.* **128**, 080505 (2022).
- [60] O. Higgott and C. Gidney, "Sparse Blossom: Correcting a Million Errors per Core Second with Minimum-Weight Matching," arXiv:2303.15933.
- [61] S. C. Smith, B. J. Brown, and S. D. Bartlett, "A local pre-decoder to reduce the bandwidth and latency of quantum error correction," *Phys. Rev. Appl.* **19**, 034050 (2023).
- [62] L. Caune *et al.*, "Belief Propagation as a Partial Decoder," arXiv:2306.17142.
- [63] J. Bausch *et al.*, "Learning high-accuracy error decoding for quantum processors," *Nature* (2024).
- [64] R. S. Gupta *et al.*, "Encoding a magic state with beyond break-even fidelity," *Nature* **625**, 259 (2024).
- [65] E. H. Chen *et al.*, "Calibrated decoders for experimental quantum error correction," *Phys. Rev. Lett.* **128**, 110504 (2022).
- [66] E. T. Hockings, A. C. Doherty, and R. Harper, "Scalable Noise Characterisation of Syndrome Extraction Circuits with Averaged Circuit Eigenvalue Sampling," arXiv:2404.06545.
- [67] C. Gidney and M. Ekerå, "How to factor 2048 bit RSA integers in 8 hours using 20 million noisy qubits," *Quantum* **5**, 433 (2021).
- [68] S. Bravyi *et al.*, "High-threshold and low-overhead fault-tolerant quantum memory," *Nature* **627**, 778 (2024).
- [69] C. A. Pattison, A. Krishna, and J. Preskill, "Hierarchical Memories: Simulating Quantum LDPC Codes with Local Gates," arXiv:2303.04798.
- [70] D. Ruiz *et al.*, "LDPC-Cat Codes for Low-Overhead Quantum Computing in 2D," arXiv:2401.09541.
- [71] M. Mohseni *et al.*, "How to Build a Quantum Supercomputer: Scaling Challenges and Opportunities," arXiv:2411.10406.

Code availability

https://github.com/YanivKurman/factorization_paper_simulations